


## Influence of imperfections on tunneling rate in $\delta$ -layer junctions

Juan P. Mendez<sup>1</sup>,\* Shashank Misra, and Denis Mamaluy<sup>1</sup>†  
 Sandia National Laboratories, Albuquerque, New Mexico 87123, USA

 (Received 15 March 2023; revised 27 June 2023; accepted 5 October 2023; published 8 November 2023)

The atomically precise placement of dopants in semiconductors using scanning tunneling microscopes has been used to create planar dopant-based devices, enabling the exploration of novel classical or quantum computing concepts, which often require precise control over tunneling rates in their operation. While the geometry of the dopants can be defined to subnanometer precision, imperfections can still play a significant role in determining the tunneling rates. Here we investigate the influence of different imperfections in phosphorus  $\delta$ -layer tunnel junctions in silicon: variations of  $\delta$ -layer thickness and tunnel gap width, interface roughness, and charged impurities. It is found that while most of the imperfections moderately affect the tunneling rate, a single charged impurity in the tunnel gap can alter the tunneling rate by more than an order of magnitude, even for relatively large tunnel gaps. Moreover, it is also revealed that the tunneling rate strongly depends on the electrical charge sign of the impurity.

DOI: [10.1103/PhysRevApplied.20.054021](https://doi.org/10.1103/PhysRevApplied.20.054021)

### I. INTRODUCTION

Atomic precision advanced manufacturing (APAM) can be used to create 2D doped regions (known as  $\delta$  layers) in silicon that simultaneously have single-atom precision [1–6] and very high conductivity [7–12]. APAM has application for exploring basic principles of novel electronic devices, including nanoscale diodes and transistors for classical computing and sensing systems [11,13–15] [see, e.g., Figs. 1(a) and 1(b)]. Primarily, however, this technology is used to explore dopant-based qubits in silicon, with recent advancements in understanding exchange-based 2-qubit operations [16], the limits to qubit fidelity from environmental noise [17], the advantages to leveraging the number of dopants as a degree of freedom [18,19], and the exploration of many-body [20] and topological [21] effects in dopant chains [see, e.g., Fig. 1(c)]. In principle, atomically precise fabrication imbues the kind of control required by these applications, which have a high sensitivity to tunneling rates.

However, in reality, APAM involves trade-offs between a number of defect mechanisms whose impact on tunneling rates have not been systematically studied, and this work pursues. A general processing trade-off exists where the point-defect density can be reduced by increasing the various processing temperatures, at the expense of lower dopant-placement uncertainty from activating dopant diffusion [10]. More specifically, there is a well-known intrinsic stochasticity from the underlying chemistry resulting in

a dopant-placement uncertainty of  $\pm 0.3$  nm [1,4]. Moreover, after dopant incorporation,  $\delta$  layers must be capped with silicon at a moderate temperature to protect them, but adatom-mediated diffusion can lead to a loss of out-of-plane sharpness that is on the order of 1 nm [22]. In contrast, the low-temperature capping-layer growth also leads to charged point defects at a density of approximately one defect in a volume of  $(10 \text{ nm})^3$  [23]. Determining which of these disorder mechanisms is most likely to create large variations in tunneling rates in a simpler tunnel-junction geometry will help inform how to navigate these trade-offs, and lays the groundwork to analyze the more-complicated case of qubits in the future.

Electron tunneling is understood in different terms at different length scales—ranging from semiempirical descriptions of resonant tunnel diodes in terms of effective barrier heights [24] to atomistic hopping through single molecules in break junctions [25]. Challenges arise in problems where the macroscale description of tunneling in terms of band structure cannot account for atomic-scale details by simply renormalizing parameters. A direct quantum mechanical way to investigate tunneling requires an open-system charge-transport treatment [26]. In this work we use an efficient, charge-self-consistent, quantum transport implementation of the open-system nonequilibrium-Green-function (NEGF) formalism, known as the “contact-block-reduction (CBR) method” [27–34]. We combine it with an effective-mass description for free electrons, shown to be in very good agreement with tight-binding models for Si nanowires with sizes down to 3 nm [35,36] and P  $\delta$ -layer tunnel junctions in Si (Si:P  $\delta$ -layer tunnel junctions) [37], to assess the effect of imperfections on the

\*jpmende@sandia.gov

†mamaluy@sandia.gov

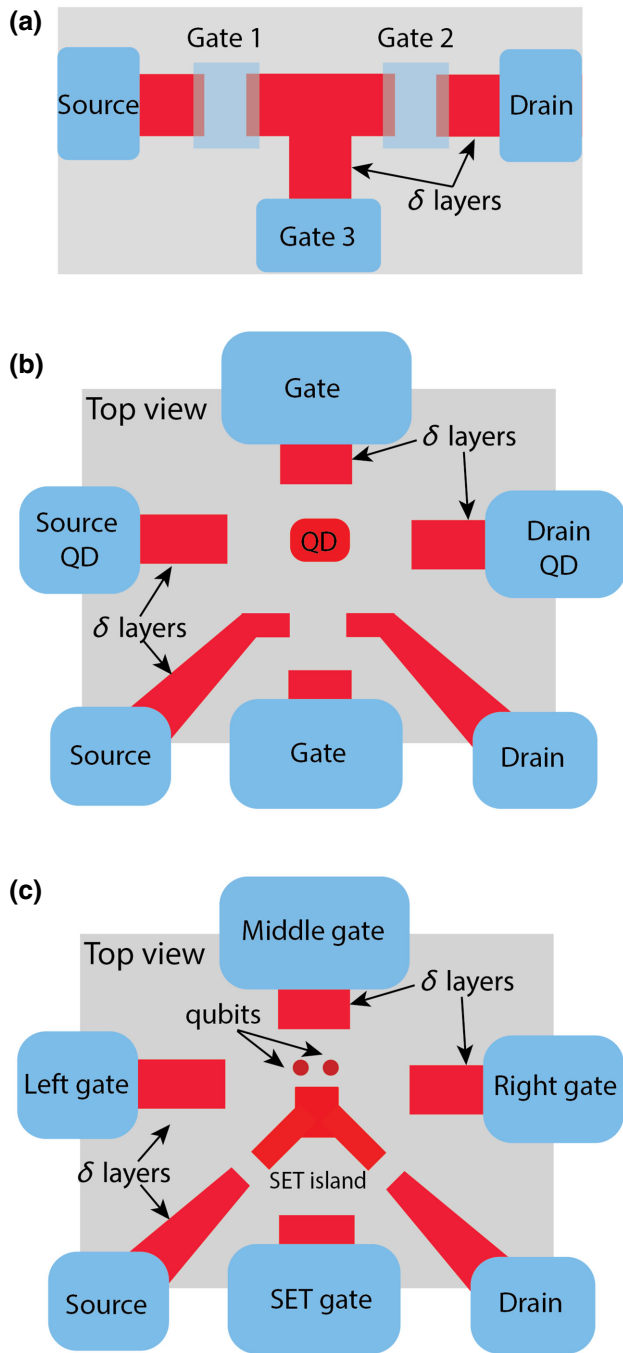


FIG. 1. Examples of atomic-precision-advanced-manufacturing nanodevices. (a)  $\delta$ -layer tunnel-junction field-effect transistor (FET) introduced by Donnelly *et al.* [15]. (b) A  $\delta$ -layer tunnel junction is used for detecting electrons in the quantum dot (QD) in Ref. [14]. (c) Two-qubit-donor spin device from Refs. [16,17]. SET, single-electron transistor.

tunneling rate for Si:P  $\delta$ -layer tunnel junctions. The imperfections considered in this work include variations of the  $\delta$ -layer thickness, small variations of the tunnel-junction gap length, roughness at the edges of the  $\delta$  layers, and the presence of charged impurities in the intrinsic gap.

## II. METHODS

To explore the impact of these defect mechanisms, we adopt a structure of a  $\delta$ -layer tunnel junction that consists of two highly conductive  $\delta$  layers separated by an intrinsic semiconductor gap. In the open-system NEGF framework, the computational device consists of a semi-infinite source and drain in contact with a channel of length  $L$ , which is composed of a lightly doped Si body and Si cap and two very thin, highly-P-doped layers (referred to as “left and right  $\delta$  layers”) separated by an intrinsic gap of length  $L_{\text{gap}}$ , as shown in Fig. 2(a). The channel length  $L$  is chosen to be  $30 \text{ nm} + L_{\text{gap}}$  to avoid the boundary effect between the source and drain contacts, the device height  $H$  is 8 nm, and the total device width  $W$  is chosen to be 15 nm, with an effective width of 12 nm for the  $\delta$  layer, to avoid size-quantization effects on the conductive properties of  $\delta$ -layer systems [38]. We consider three different  $\delta$ -layer thicknesses:  $t = 0.2 \text{ nm}$  to approximate the true monoatomic  $\delta$  layer, intermediate  $t = 1.0 \text{ nm}$ , and a “thick”  $\delta$  layer with  $t = 5.0 \text{ nm}$ . The sheet doping density  $N_D$  of the  $\delta$  layer is  $1.0 \times 10^{14} \text{ cm}^{-2}$  ( $N_D^{(2D)} = t \times N_D^{(3D)}$ ) and the doping densities  $N_A$  in the Si cap and Si body are  $5.0 \times 10^{17} \text{ cm}^{-3}$  in all simulations. In Ref. [39], it was found that the effect of dopant disorder or order in the  $\delta$  layers is negligible; thus, modeling the  $\delta$  layer as a continuum steplike doping profile is a good approximation. Furthermore, all simulations are performed at the cryogenic temperature of 4 K, for which we can ignore inelastic scattering [7,40].

The simulations in this work are conducted with the open-system charge-self-consistent NEGF Keldysh formalism [41,42], together with the CBR method [27–34] and the effective-mass theory. The CBR method allows very-efficient calculation of the density matrix, transmission function, etc. of an arbitrarily shaped, multiterminal 2D or 3D open device within the NEGF formalism and scales linearly  $O(N)$  with the system size  $N$ . As validation, in our previous work [43,44], we demonstrated very good agreement with experimental electrical measurements for Si:P  $\delta$  layer systems [7,45–47], proving excellent reliability of this framework to investigate  $\delta$ -layer systems. Similarly, our results in Ref. [38], without fitting parameters, agree remarkably well with the most-recent experimental data for tunnel junctions in these systems [48], as exhibited in Ref. [37].

Within this framework, we solve self-consistently the open-system effective-mass Schrödinger equation and the nonlinear Poisson equation [27,30,33]. We use a single-band effective-mass approximation with valley degeneracy  $d_{\text{val}} = 6$ . For the charge-self-consistent solution of the nonlinear Poisson equation, we use a combination of the predictor-corrector approach and the Anderson mixing scheme [31,33]. First, the Schrödinger equation is solved in a specially defined closed-system basis by basis by taking into account the Hartree potential  $\phi^H(\mathbf{r}_i)$  and the

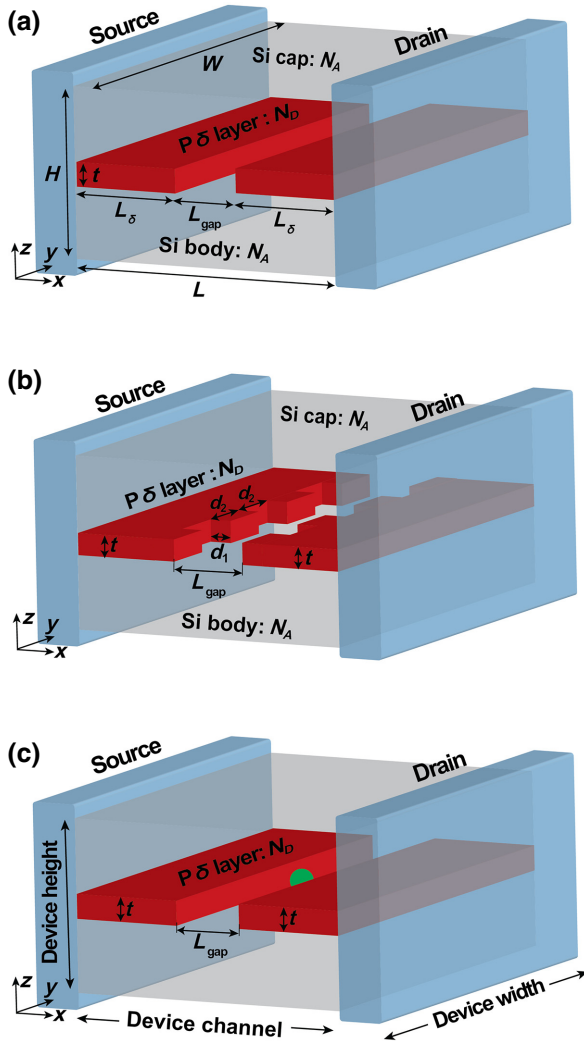


FIG. 2. Si:P  $\delta$ -layer tunnel-junction devices. (a) Ideal device, which consists of a semi-infinite source and drain in contact with the channel. The channel is composed of a lightly doped Si body and Si cap and a very thin, highly-P-doped layer with an intrinsic gap of length  $L_{\text{gap}}$ . (b) Device with roughness in  $\delta$ -layer edges. The edge roughness is modeled as periodic protrusions of size  $d_1 \times d_2 \times t$  with periodicity of  $2d_2$ . (c) Device with the presence of a charged impurity, either  $p$  type or  $n$  type, in the center of the intrinsic tunnel gap. The charged impurity is represented as a green sphere.

exchange-and-correlation potential  $\phi^{XC}(\mathbf{r}_i)$  [49]. Second, the local density of states (LDOS) of the open system,  $\rho(\mathbf{r}_i, E)$ , and the electron density,  $n(\mathbf{r}_i)$ , are computed with use of the CBR method for each iteration. Then the electrostatic potential and the carrier density are used to calculate the residuum  $F$  of the Poisson equation:

$$\|F[\phi^H(\mathbf{r}_i)]\| = \|A\phi^H(\mathbf{r}_i) - (n(\mathbf{r}_i) - N_D(\mathbf{r}_i) + N_A(\mathbf{r}_i))\|, \quad (1)$$

where  $A$  is the matrix derived from the discretization of the Poisson equation and  $N_D$  and  $N_A$  are the total donor and acceptor doping density arrays, respectively. If the residuum is larger than a predetermined threshold  $\epsilon$ , the Hartree potential is updated with use of the predictor-corrector method, together with the Anderson mixing scheme. With use of the updated Hartree potential and the corresponding carrier density, the exchange-correlation is computed again for the next step, and an iteration of the Schrödinger-Poisson equations is repeated until convergence is achieved with  $\|F[\phi^H(\mathbf{r}_i)]\| < \epsilon = 10^{-6}$  eV. Further details of the method are included in Ref. [37]. In our simulations we have used a 3D real-space model, with a discretization size of 0.2 nm along all directions, thus with about  $10^6$  real-space grid points, and around 3000 energy points. The CBR algorithm automatically ascertains that of more than 1 000 000 eigenstates, only about 700 (less than 0.1%) of lowest-energy states are needed, which is generally determined by the material properties (e.g., doping level), but not the device size. We also use the standard values of the inertial-effective-mass tensor for electrons,  $m_l = 0.98 \times m_e$  and  $m_t = 0.19 \times m_e$ , and the dielectric constant of silicon,  $\epsilon_{\text{Si}} = 11.7$ .

### III. RESULTS AND DISCUSSION

#### A. Conductivity of ideal tunnel junctions

In our previous work for infinite-width ( $W \rightarrow \infty$ )  $\delta$ -layer systems [44], we demonstrated that the distribution of dopants along the confinement  $z$  axis for a fixed sheet doping density ( $N_D^{(2D)}$ ) significantly affects the current. Conductivity decreases for sharper  $\delta$ -layer doping profiles, which create strong transverse electric fields in their vicinity, while it increases for broader  $\delta$ -layer doping profiles, which conversely create weaker transverse electric fields. We also report in this work that the same trend is observed for finite-width  $\delta$ -layer tunnel junctions. In Fig. 3, the tunneling current  $I$  versus the tunnel gap length  $L_{\text{gap}}$  for an ideal  $\delta$ -layer tunnel junction [see Fig. 2(a)] is included for different  $\delta$ -layer thicknesses and two voltages: 1 and 100 mV. As shown, the tunneling current decreases as the  $\delta$ -layer thickness decreases for a fixed sheet doping density (i.e., the total charge density is kept constant). We also find that the overall  $I$ -versus- $L_{\text{gap}}$  trend is practically exponential for all tunnel gap lengths  $L_{\text{gap}} = 0, \dots, 12$  nm, i.e.,  $\ln I \sim \ln I_{L_{\text{gap}}=0} - L_{\text{gap}}/B_{\text{voltage}}$ , where  $I_{L_{\text{gap}}=0}$  is the current when  $L_{\text{gap}} = 0$ ,  $L_{\text{gap}}$  is the tunnel gap length, and  $B_{\text{voltage}}$  is a proportional constant related to the barrier height. As a guide for the eye, the exponential  $I$ -versus- $L_{\text{gap}}$  trend is included in Fig. 3 as dotted black lines for  $t = 1$  nm. However, deviation from the exponential trend can be noticed for large tunnel gaps  $L_{\text{gap}} > 7$  nm and an applied voltage of 1 mV (dashed black lines). Conversely, for a voltage of 100 mV (continuous lines in Fig. 3), the deviation from

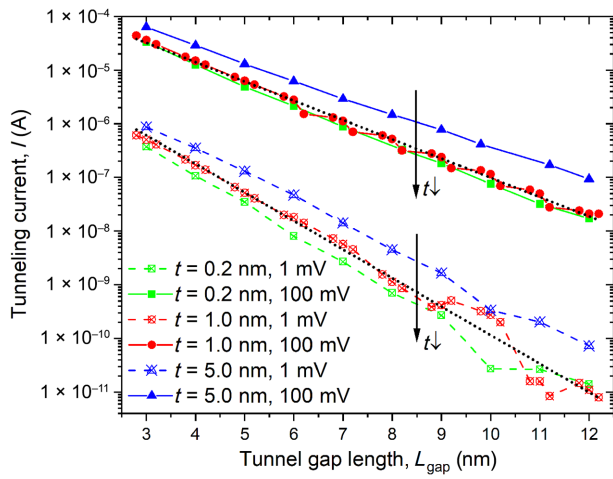


FIG. 3. Characteristic tunneling-current curves. Total current  $I$  (semilogarithmic scale) versus tunnel gap length  $L_{\text{gap}}$  for different  $\delta$ -layer thicknesses  $t$  and applied voltages (1 and 100 mV). Dotted black lines represent least-squares fits to the exponential trend.  $N_D = 1.0 \times 10^{14} \text{ cm}^{-2}$  and  $N_A = 5.0 \times 10^{17} \text{ cm}^{-3}$ .

the ideal trend vanishes and the overall trend is exponential, thus shedding light on two conductivity regimes for  $\delta$ -layer tunnel junctions [38]: low-voltage and high-voltage regimes. As reported in Ref. [38], the deviation from the ideal trend is the result of the quantized conduction band in both  $\delta$  layers (left and right) and a certain mismatch between the left and right states, which importantly can occur only for low applied voltages.

Figure 4 shows the  $I$ - $V$  curve for an ideal tunnel junction of length  $L_{\text{gap}} = 10 \text{ nm}$  and  $t = 1 \text{ nm}$ . We can discern two Ohmic behaviors, elucidating again the existence of two distinct conductivity regimes corresponding to low and high voltage: the first one, between 0 and 0.04 V, with a resistance of approximately 5–6 M $\Omega$ ; the second one, above 0.08 V, with a resistance of 0.2–0.3 M $\Omega$ . The resistance in the low-voltage regime is 1 order of magnitude higher than that in the high-voltage regime. Between these two regimes, approximately between 0.04 and 0.08 V, there is a transition region over which the resistance is reduced. The tunneling resistance in the low-bias regime agrees very well with the measured resistances for tunnel junctions in Ref. [48] for the same regime [37]. Additionally, we note that the existence of two conductivity regimes in  $\delta$ -layer tunnel junctions agrees well with recent experimental  $I$ - $V$  measurements [15,48].

To get a better understanding of the two conductivity regimes (see Fig. 4) and the strong influence of the quantized conduction band on the tunneling current for low voltages (see the oscillations for  $L_{\text{gap}} > 7 \text{ nm}$  in Fig. 3), we examine the local density of states (LDOS), which represents the available states that can be occupied by the free electrons in the space-energy dimension. For very low temperatures, the states below the Fermi level are

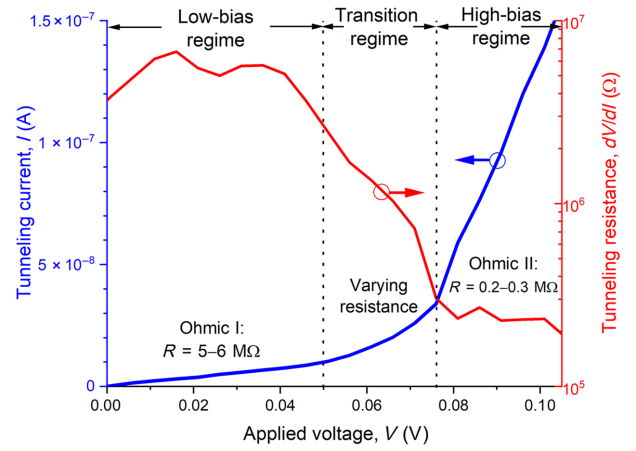


FIG. 4. Two conductivity regimes in  $\delta$ -layer tunnel junctions. Total current versus voltage (blue curve, linear scale) and the corresponding differential resistance  $dV/dI$  (red curve, semilogarithmic scale) are shown for  $L_{\text{gap}} = 10 \text{ nm}$ ,  $N_D = 1.0 \times 10^{14} \text{ cm}^{-2}$ ,  $N_A = 5.0 \times 10^{17} \text{ cm}^{-3}$ , and  $t = 1 \text{ nm}$ .

occupied, whereas the states above the Fermi level are unoccupied. Figure 5 shows the LDOS along the  $x$  direction for a tunnel junction of  $L_{\text{gap}} = 10 \text{ nm}$  when voltages of 1 mV [Fig. 5(a)] and 100 mV [Fig. 5(b)] are applied to the drain contact. Additionally, the corresponding effective 1D potential is included in Fig. 5, exhibiting a tunnel barrier height of approximately 55 meV for the equilibrium case, which is in excellent agreement with the estimated height obtained from the measured  $I$ - $V$  curve obtained with the WKB approximation for direct tunneling resistance [15] and the tight-binding calculations for the barrier height in Ref. [48]. Firstly, as shown in Fig. 5, the low-energy LDOS is strongly quantized, highlighted with dashed lines in Fig. 5. This strong quantization (or similarly the presence of quasidiscrete states) at low energies is the result of the strong confinement of the electrons in the  $z$  direction due to the ultrathin  $\delta$  layer. The presence of discrete states has been observed experimentally in several high-resolution angle-resolved photoemission spectroscopy measurements for  $\delta$  layers in silicon [50,51]. In contrast, for high energies, the LDOS is practically continuous in the real space and energy dimensions, and thus these states are not quantized. When a voltage is applied to the drain contact, the Fermi level corresponding to the drain contact is reduced, resulting in lowering of the energies of all states on the right side as well. As a result, new unoccupied states in the right  $\delta$  layer will be available for occupation by the tunneling electrons coming from the left  $\delta$  layer. When a low drain voltage is applied, e.g. less than 50 mV, only the unoccupied quantized states in the right  $\delta$  layer will play a role in the tunneling process. If the occupied quasidiscrete states near the Fermi level on the left side align with the unoccupied quasidiscrete states on the right side, this will result in a considerable increase of the tunneling current, as shown

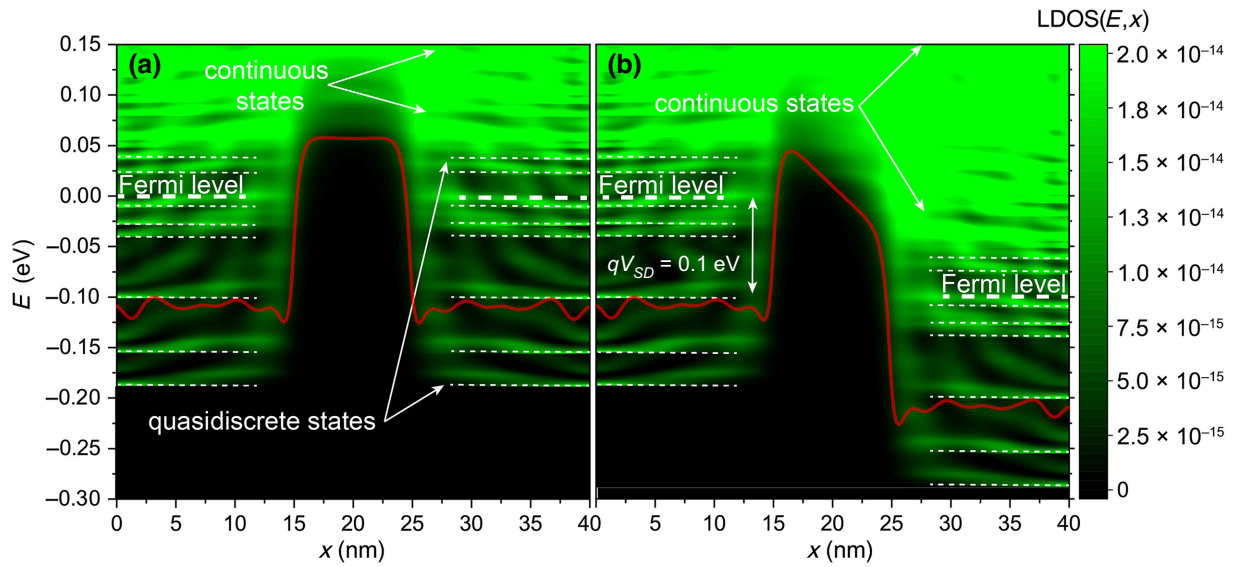


FIG. 5. Local density of states for  $\delta$ -layer tunnel junctions is shown in (a),(b) when voltages of 1 and 100 mV are applied to the drain contact, respectively. The Fermi levels indicated correspond to the Fermi levels of the source and drain contacts. The corresponding effective 1D potentials are also shown, calculated by integrating over the  $y$ - $z$  plane the actual charge-self-consistent 3D potentials weighted with the electron density.  $L_{\text{gap}} = 10$  nm,  $N_D = 1.0 \times 10^{14}$  cm $^{-2}$ ,  $N_A = 5.0 \times 10^{17}$  cm $^{-3}$ , and  $t = 1$  nm.

in Fig. 3 for  $L_{\text{gap}} = 10$  nm and  $t = 1$  nm. Conversely, if the overlap is minimum, as happens for  $L_{\text{gap}} = 11$  nm and  $t = 1$  nm, the tunneling current will be reduced. For low biases, this alternating mismatch can exist only for sufficiently large tunnel gaps,  $L_{\text{gap}} > 7$  nm, because the coupling of the wave functions of the left and right  $\delta$ -layers for narrow tunnel gaps ( $L_{\text{gap}} < 7$  nm) equalizes the electron states on both sides, increasing the overlap and thus eliminating the mismatch. When a high bias is applied, as in the case in Fig. 5(b), this makes the continuous unoccupied high-energy states on the right side available for tunneling from the left side, thus diminishing the influence of the conduction-band quantization on the current, as can be seen in  $I$ -versus- $L_{\text{gap}}$  plots in Fig. 3 for 100 mV.

In the following we evaluate the effect of diverse imperfections in  $\delta$ -layer tunnel junctions on the tunneling current. We note the importance of the evaluation of the tunneling rate for both conductivity regimes: low-voltage and high-voltage regimes. For low voltages, strong quantization effects on the tunneling current are expected, especially for large tunnel gaps, because of the quantized low-energy conduction band; thus, it will be reflected in nonmonotonic or oscillating  $I$ - $V$  curves. Conversely, in the high-bias regime, no significant influence of the conduction-band quantization is expected on the tunneling current.

### B. Effects of variation of $\delta$ -layer thickness from a monoatomic layer

We first investigate the effects of variation of  $\delta$ -layer thickness on the tunneling rate. Figure 6 shows the current

ratio between two different  $\delta$ -layer thicknesses ( $t = 1$  nm and  $t = 5$  nm) with respect to the ideal monoatomic layer, which is approximately 0.2 nm, as dashed lines for a low bias of 1 mV and as continuous lines for a high bias of 100 mV. Our results suggest that the tunneling rate increases by approximately up to 2 times for a broadening of the  $\delta$  layer of 1 nm. Interestingly, the effect is roughly constant for the whole tunnel-gap  $L_{\text{gap}}$  range considered. However, for even wider  $\delta$  layers, the tunneling rate further

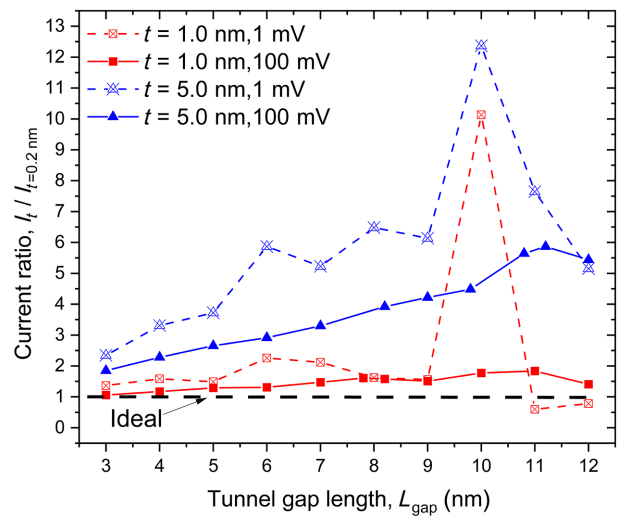


FIG. 6. Effect of variation of  $\delta$ -layer thickness. Current ratio,  $I_t / I_{t=0.2 \text{ nm}}$ , versus tunnel gap length for different deviations of the  $\delta$ -layer thickness from the “ideal” monoatomic layer.

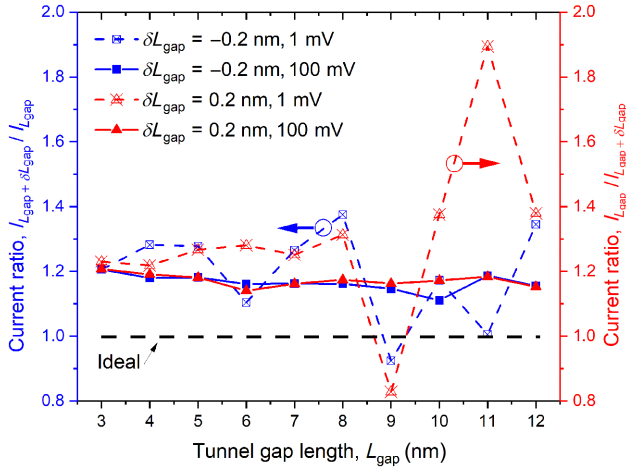


FIG. 7. Effect of variation of tunnel gap length. Current ratio,  $I_{L_{\text{gap}} + \delta L_{\text{gap}}} / I_{L_{\text{gap}}}$  versus tunnel gap length,  $L_{\text{gap}}$ , for different applied voltages.  $t = 1.0$  nm,  $N_D = 1.0 \times 10^{14}$  cm $^{-2}$ , and  $N_A = 5.0 \times 10^{17}$  cm $^{-3}$ .

increases, by between 2 and 7 times for a effective thickness of 5 nm, developing now a stronger dependence on the tunnel gap length. Furthermore, for large tunnel gaps in the low-bias regime (1 mV), the strong nonmonotonic dependence of the current ratio on the gap length is the result of the space-energy quantization of the conduction band and the mismatch in the overlap between the states in the left and right  $\delta$  layers, as discussed in Sec. III A. More specifically, the peak at  $L_{\text{gap}} = 10$  nm is the result of maximum overlap between occupied quasidiscrete states from the left  $\delta$  layer and unoccupied quasidiscrete states from the right  $\delta$  layer for  $\delta$  layers thicker than monoatomic layers. It is worth noting that the energy levels of these quasidiscrete states exhibit a dependence on multiple factors, including the doping density, width and thickness, and length of the tunnel gap. When a higher voltage is applied (e.g., 100 mV), this results in a lower current ratio, and the quantization effects diminish as we discussed in Sec. III A.

### C. Effects of variation of the tunnel gap length and interface roughness

Next we assess how the variation of the tunnel gap length and the roughness of the  $\delta$  layer might affect the tunneling rate. As a first approximation, the interface roughness can be modeled as a uniform increase or reduction of the average gap length  $\langle L_{\text{gap}} \rangle$ . We evaluate in Fig. 7 the change in the tunneling current for small uniform variations, such as  $L_{\text{gap}} + \delta L_{\text{gap}}$ , with  $\delta L_{\text{gap}} = \pm 0.2$  nm. This small perturbation is on the order of the stochasticity of APAM chemistry. Our simulations suggest that a small variation of the tunnel gap length (on the order of  $\pm 0.2$  nm) can lead to a current change of around 20% with respect to the ideal (or designed) length for the whole range studied. A reduction of the tunnel gap length evidently results in

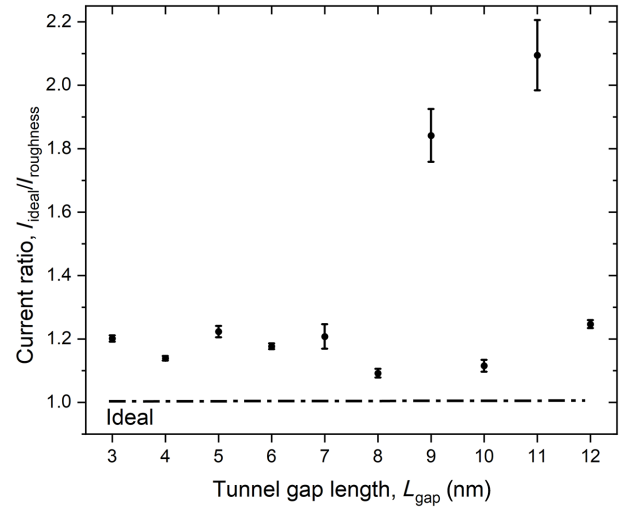


FIG. 8. Effect of interface roughness. Current ratio,  $I_{\text{ideal}} / I_{\text{roughness}}$ , versus tunnel gap length,  $L_{\text{gap}}$ , for an applied bias of 1.0 mV. For each tunnel gap length, different degrees of roughness are considered, ranging from  $d_1 = 0.8$  nm to  $d_1 = 2.0$  nm and from  $d_2 = 0.6$  nm to  $d_2 = 3.4$  nm [see Fig. 2(b)]. The dots represent the average and the bars represent the dispersion of the values.  $t = 1.0$  nm,  $N_D = 1.0 \times 10^{14}$  cm $^{-2}$ , and  $N_A = 5.0 \times 10^{17}$  cm $^{-3}$ .

an increase of the tunneling rate, while an increase of the effective gap length leads to a decrease of the tunneling rate by a similar magnitude. For large tunnel gaps in the low-bias regime (see the dashed lines for 1 mV), our results similarly present the expected nonmonotonic behavior due to the quantization effect, but this effect vanishes when a higher voltage is applied (see the continuous lines for 100 mV).

A second-order analysis of the edge roughness can be performed assuming that the average  $\langle L_{\text{gap}} \rangle$  value does not change due to the roughness. In this case, we model the roughness as a periodic protrusion of size  $d_1 \times d_2 \times t$ , with periodicity of  $2d_2$ , as shown in Fig. 2(b), instead of the uniform variation evaluated above. To maintain  $\langle L_{\text{gap}} \rangle$  constant, we consider only in-phase roughness, i.e., the protrusion of the left  $\delta$  layer is exactly a mirror of the right side. The analysis of out-of-phase roughness is not within the scope of this work, and it will be further investigated elsewhere. In our analysis, we consider different degrees of roughness, by varying  $d_1$  from 0.8 to 2.0 nm and by varying  $d_2$  from 0.6 to 3.4 nm. Figure 8 includes, for all degrees of roughness evaluated, the current ratio between the “nonideal” tunnel-junction device (with edge roughness) and the “ideal” device (without any roughness) for a voltage of 1 mV. The simulations indicate that edge roughness reduces the tunneling rate by between 6% and 20% for almost the whole gap range considered, predicting a very similar magnitude of the tunneling-rate change as the uniform variation of the tunnel gap length. One can also notice

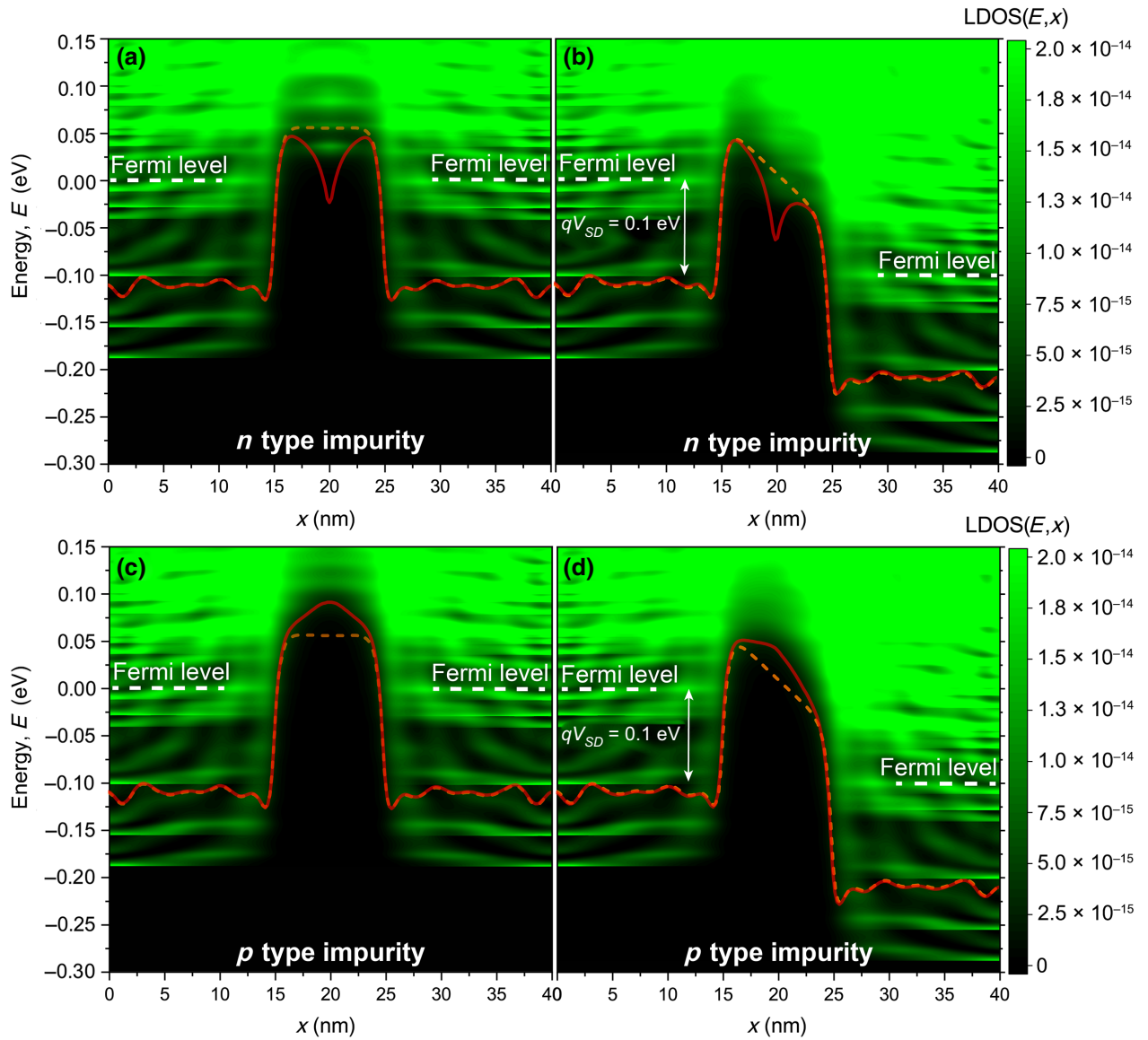


FIG. 9. Local density of states for  $\delta$ -layer tunnel junctions with charged impurities in the middle of the junction is shown: for a single  $n$ -type impurity when voltages of 1 and 100 mV are applied to the drain contact in (a),(b), respectively; for a single  $p$ -type impurity when voltages of 1 and 100 mV are applied in (c),(d), respectively. In all plots, the corresponding effective 1D potentials are also shown in red, calculated by integrating over the  $y$ - $z$  plane the actual charge-self-consistent 3D potentials weighted with the electron density. The effective 1D potential for the ideal tunnel junction is also included as dashed orange lines for comparison.  $L_{\text{gap}} = 10$  nm,  $t = 1.0$  nm,  $N_D = 1.0 \times 10^{14}$  cm $^{-2}$ , and  $N_A = 5.0 \times 10^{17}$  cm $^{-3}$ .

that for large tunnel gaps, especially for  $L_{\text{gap}} = 9$ – $10$  nm, the tunneling rate is even further reduced by up to 2.2 times due to the aforementioned quantization of the conduction band.

#### D. Effects of charged impurities in the tunnel gap

In the following, we evaluate the effects of a single charged impurity in the tunnel gap on the tunneling rate, assuming a point-charge distribution for all charged impurities regardless of the specific atomic species, as shown in

Fig. 2(c). For the simulation setup, we place in the center of the tunnel gap either an  $n$ -type impurity (e.g., a phosphorus atom) or a  $p$ -type impurity (e.g., an aluminum atom). The impurities are modeled by approximating a point charge with a density of (positive or negative)  $4.6 \times 10^{21}$  cm $^{-3}$  homogeneously distributed in a total volume of  $(0.6 \text{ nm})^3$ . While in this work we restrict our analysis to the center-gap location, the influence of other locations may be also interesting to investigate since the free electrons in  $\delta$ -layer systems form distinct conducting layers perpendicular to the confinement direction, thus signaling

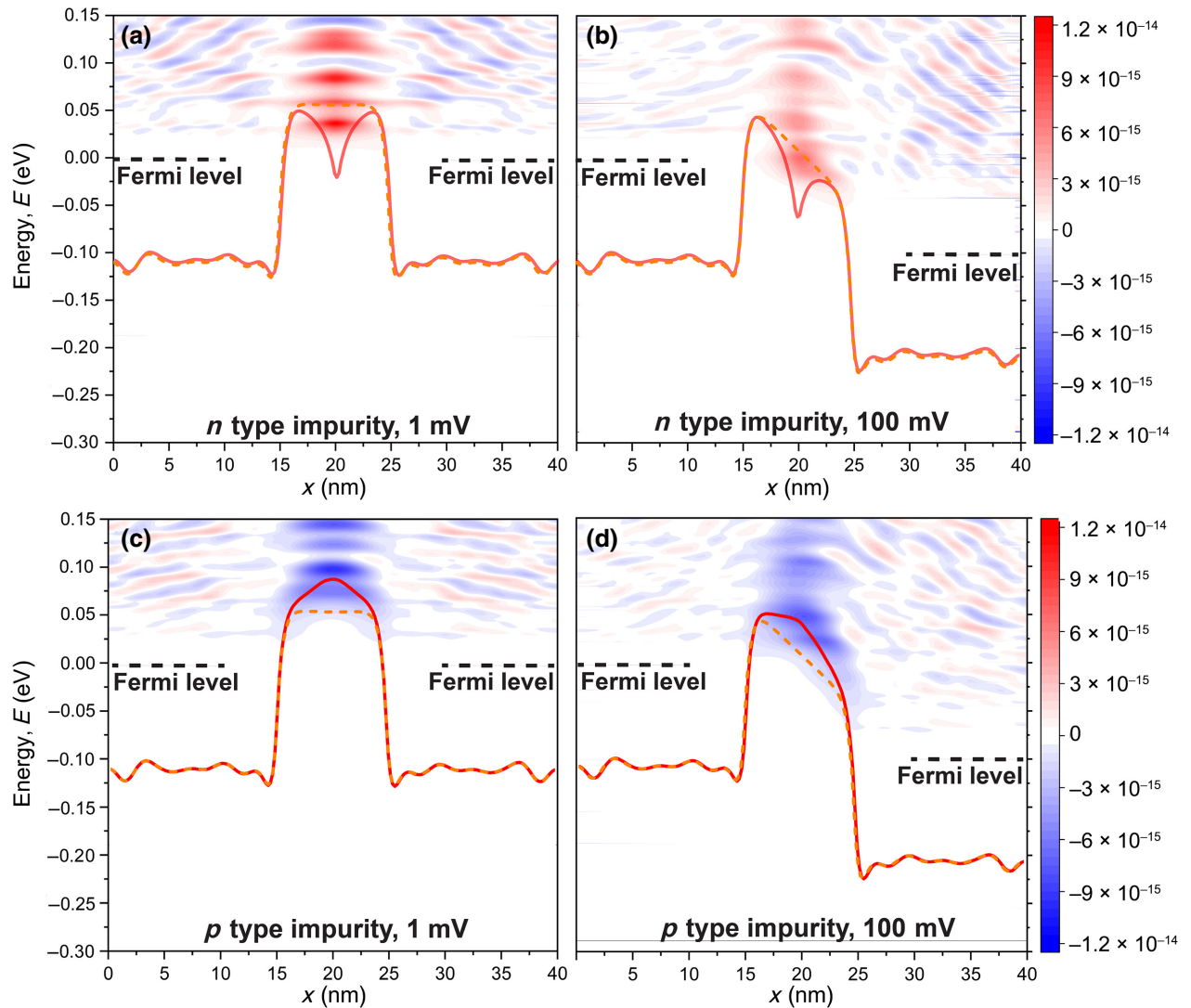


FIG. 10. Localized states created or depleted by charged impurities are shown: for a single  $n$ -type impurity in the middle of the tunnel in (a),(b) for applied voltages of 1 and 100 mV, respectively; for a single  $p$ -type impurity for applied voltages of 1 and 100 mV in (c),(d), respectively. The plots represent the difference of the local density of states, i.e. between the device with and the device without the impurity. The corresponding effective 1D potentials are also shown in red, together with the effective 1D potential for the ideal case in orange.  $L_{gap} = 10$  nm,  $N_D = 1.0 \times 10^{14}$  cm $^{-2}$ ,  $N_A = 5.0 \times 10^{17}$  cm $^{-3}$ , and  $t = 1$  nm.

a highly nonhomogeneous electron-density distribution [43,44].

Figure 9 shows the LDOS of a  $\delta$ -layer tunnel junction with a single  $n$ -type impurity for applied voltages of 1 mV [Fig. 9(a)] and 100 mV [Fig. 9(b)] and with a single  $p$ -type impurity for applied voltages of 1 mV [Fig. 9(c)] and 100 mV [Fig. 9(d)]. Figure 10 shows the LDOS difference for both applied voltages between the ideal tunnel junction (i.e., the LDOS shown in Fig. 5) and the junction with the impurity (i.e., the LDOS shown in Fig. 9); therefore, it represents the localized states created (in red) or depleted (in blue) by the impurity. As Figs. 9(a) and 9(b) reveal, an  $n$ -type impurity in the middle of the tunnel gap creates unoccupied states above the Fermi level within the tunnel

gap region, i.e., between  $x = 15$  nm and  $x = 25$  nm, as one might discern by comparing Figs. 5(a) and 9(a) and Figs. 5(b) and 9(b). The new available states are clearly shown in red in Figs. 10(a) and 10(b). In contrast, a  $p$ -type impurity depletes unoccupied available states above the Fermi level as shown in Figs. 9(c) and 9(d) within the tunnel gap region ( $x = 15$ – $25$  nm). The depletion of the states due a  $p$ -type impurity can be also seen in Figs. 10(c) and 10(d) in blue since we are representing the LDOS difference between the ideal tunnel junction and the tunnel junction with the  $p$ -type impurity. The impurity creates a quantized perturbation in the unoccupied states (above the Fermi level) even far from the impurity location, shown as ripples between  $x = 0$  nm and  $x = 15$  nm and between



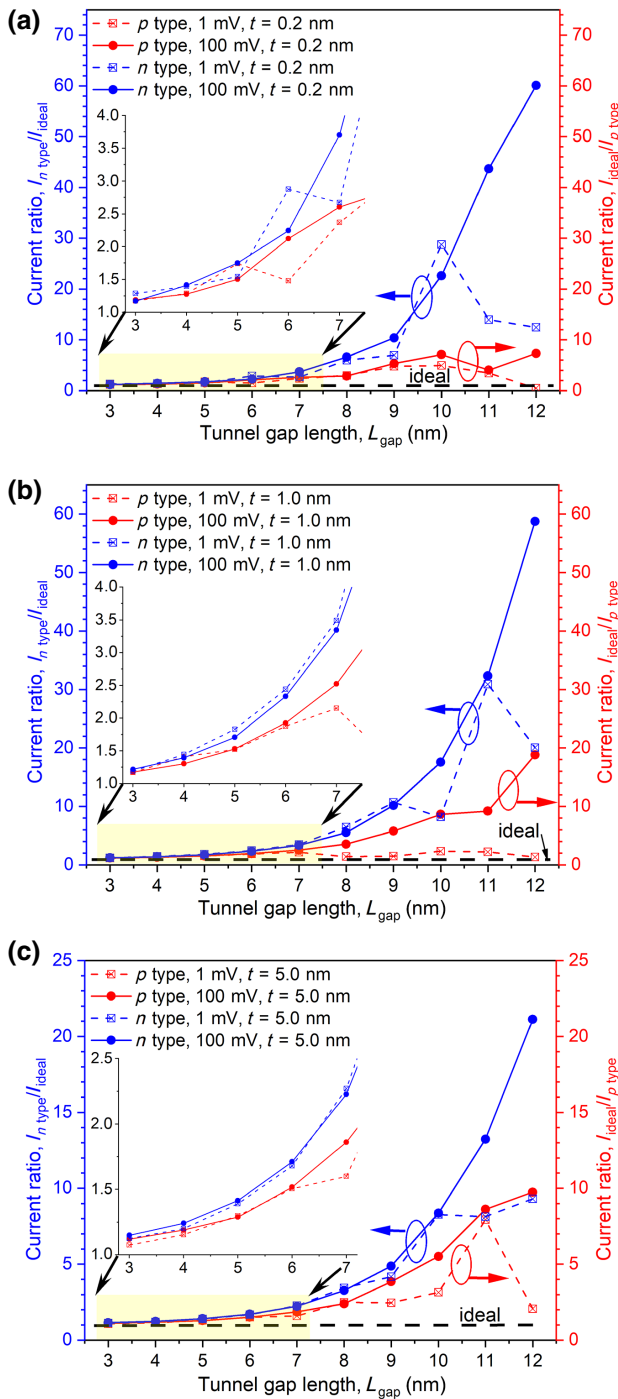


FIG. 11. Effect of charged impurities. Current ratio,  $I_{\text{non-ideal}}/I_{\text{ideal}}$ , versus tunnel gap length,  $L_{\text{gap}}$ , for tunnel junctions with a single  $n$ -type impurity and a single  $p$ -type impurity in the intrinsic gap: (a)  $t = 0.2$  nm; (b)  $t = 1.0$  nm; and (c)  $t = 5.0$  nm. The insets show an enlargement of the results in the range between 3 and 8 nm.  $N_D = 1.0 \times 10^{14} \text{ cm}^{-2}$  and  $N_A = 5.0 \times 10^{17} \text{ cm}^{-3}$ .

$x = 25$  nm and  $x = 40$  nm above the Fermi level in Fig. 10. However, the perturbations vanish as we move away from the impurity location.

In the semiclassical picture, the energy difference between the peak of the effective electrostatic potential and the Fermi level is the energy barrier that the electrons have to overcome to tunnel from one  $\delta$  layer to the other. Because of the presence of the impurity in the middle of a nanoscale gap, the effective electrostatic potential is obviously affected. For an  $n$ -type impurity in the middle of a tunnel gap, the height of the electrostatic barrier is reduced, as shown in Fig. 9(a), in which the height of the electrostatic barrier without impurity (the dashed orange curve) is slightly greater than the height of the electrostatic barrier with an  $n$ -type impurity (the continuous red curve). In addition, the  $n$ -type impurity creates a dip in the electrostatic potential due to the donor atom. For a  $p$ -type impurity, acceptor atom, the depletion of the states above the Fermi level, in turn, increases the height of the energy barrier in the electrostatic potential with respect to the ideal case, as depicted in Fig. 9(c), where the height of the electrostatic potential for the ideal tunnel junction (continuous red curve) is greater than the height of the electrostatic potential for the tunnel junction with the impurity (dashed orange curve).

Figure 11 shows the current ratio versus the tunnel gap length  $L_{\text{gap}}$  for both impurity types and voltage regimes (1 and 100 mV) for  $\delta$ -layer thicknesses  $t$  of 0.2, 1.0, and 5.0 nm. These simulations first reveal that an  $n$ -type impurity increases the tunneling rate, whereas a  $p$ -type impurity decreases the tunneling rate. This result can be explained in two different, but related, ways. The first one, which corresponds to a semiclassical picture, is by examining the electrostatic potentials shown in Fig. 9 and discussed above: an  $n$ -type impurity decreases the barrier height (i.e., the energy difference between the peak of the electrostatic potential and the Fermi level), whereas a  $p$ -type impurity increases the barrier height. Then the tunneling current increases or decreases according to the change of the barrier height. The other way is to examine the unoccupied and occupied states in the LDOS for the conduction band. When we apply a positive voltage to the drain contact, the right Fermi level and occupied and unoccupied states move down, falling below the Fermi level of the source. As a result, electrons injected from the source can tunnel into these available states. The presence of an  $n$ -type impurity creates unoccupied states within the tunnel gap, just above the Fermi level in equilibrium. Similarly, when a voltage is applied, these available states might also fall within the source and drain Fermi levels and, therefore, they become intermediate states in which electrons can tunnel in and out, reducing then the tunneling length (i.e., the width of the barrier in the semiclassical picture) and, therefore, increasing the tunneling rate. In contrast, the presence of a  $p$ -type impurity creates a depletion of the states within the tunnel gap, as shown in Figs. 10(c) and 10(d) as a blue cloud around the effective electrostatic potential, increasing then

the effective tunneling length and, therefore, reducing the tunneling current.

We can also observe from Fig. 11 two different behaviors, corresponding to narrow tunnel gaps  $L_{\text{gap}} = 3\text{--}7$  nm and large tunnel gaps  $L_{\text{gap}} > 7$  nm, in which the deviation of the tunneling current from the ideal tunneling current behaves differently. For narrow tunnel gaps, the magnitude of the effect on the tunneling rate is very similar for both impurity types and not very pronounced (see the insets in Fig. 11): up to 3.75 times increase and 2.5 times reduction of the tunneling rate for an  $n$ -type and a  $p$ -type impurity, respectively, when the tunnel gap length is 7 nm. Our simulations also show that there is not a significant difference in the tunneling-rate change in both voltage regimes (1 mV for the low-voltage regime and 100 mV for the high-voltage regime) for narrow tunnel gaps: the change of the tunneling rate with respect to the ideal tunneling current is only slightly higher for higher voltages. The deviation in the magnitude of the effect on the tunneling current between both impurity types starts approximately for  $L_{\text{gap}} > 7$  nm: the effect of an  $n$ -type impurity becomes much-more relevant than the effect of a  $p$ -type impurity, especially for the high-voltage regime (100 mV in Fig. 11), in which it is a few times greater than in the low-voltage regime (1 mV in Fig. 11). Interestingly, our simulations suggest that the tunneling current can be up to 60 times higher and 20 times lower for a single  $n$ -type impurity and a single  $p$ -type impurity, respectively, for a tunnel gap length of 12 nm. Finally, we also note that the effect of charged impurities on the tunneling rate is greater in thinner  $\delta$  layers, as our results indicate an increase in the current ratio with decreasing  $\delta$ -layer thickness.

#### IV. CONCLUSION

We have used an open-system quantum transport analysis to investigate the effect of diverse imperfections on the tunneling rate in Si:P  $\delta$ -layer tunnel junctions. These imperfections range from geometry variations of the  $\delta$ -layer thickness and junction gap length to the presence of charged impurities, either  $n$  type or  $p$  type, in the intrinsic gap. It is shown that while most of the disorders moderately affect the tunneling rate, a single charged impurity in the tunnel gap can alter the tunneling rate by more than an order of magnitude. Contrary to predictions of semi-classical impurity-scattering (mobility-based) models, the electric sign of the impurity plays an important role in the tunneling rate: the rate of current increase due to an  $n$ -type impurity in Si:P  $\delta$ -layer systems is several times greater than the rate of current decrease for a  $p$ -type impurity, especially for large tunnel gap lengths. Similarly, we can extrapolate these findings to other systems, such as Si:B  $\delta$ -layer tunnel junctions, in which the influence of a  $p$ -type impurity in the intrinsic gap, instead of an  $n$ -type impurity, would result in a dramatic increase of the tunneling current.

These results immediately suggest that the overall geometric fidelity of fabrication of the APAM device can be less important than mitigation of charged impurities near the junction, which can lead to a strong change of tunneling rates. APAM-based qubits, in particular, require having tunneling rates that are tightly controlled between multiple closely spaced objects. This includes exchange coupling between a pair of donor-based qubits, initialization from a tunnel-coupled single-electron transistor, and spin-to-charge conversion from the resonant tunneling of the single-electron transistor to the leads in Fig. 1. Importantly, a change in tunneling rates from the fabricated geometry due to impurities can be hard to compensate for with use of electrostatic gates. The size of the gates (tens of nanometers) and the required spacing for them to not leak to one another (tens of nanometers) are much larger than the length scale for tunnel coupling (a few nanometers). In the APAM geometry, these gates are few in number—enough to control electrostatics, but too few to control tunneling rates. This leads to the conclusion that adopting APAM processing practices that minimize charged defects is more important than adopting practices that preserve the absolute device geometry.

Finally, it is worth noting that the extreme variation in the magnitude of the tunneling current in the presence of charges near the tunnel junction offers significant potential for use in quantum FET-based devices for sensing charges in biological, chemical, and radiation applications. The signal detection (either due to radiation or due to specific molecules) at the sensing area would be strongly enhanced due to the conduction-band quantization created by the highly confined  $\delta$  layers. The sensing area can be placed above the tunnel gap, replacing the traditional gate in a conventional geometry. In contrast to traditional FET-based sensors, instead of needing to accumulate enough charges at the sensing area to invert the full channel and detect the signal [52], quantum FETs based on  $\delta$  layers would allow one to detect even small signals that correspond to a single charge, thus significantly increasing the sensitivity with respect to traditional FET-based sensors.

#### ACKNOWLEDGMENTS

The authors thank FAIR DEAL's team at Sandia National Laboratories for discussions during the project's meetings. This work was funded under the Laboratory Directed Research and Development Grand Challenge program, Project No. 213017, and under the Laboratory Directed Research and Development program, Project No. 227155, at Sandia National Laboratories. Sandia National Laboratories is a multimission laboratory managed and operated by National Technology and Engineering Solutions of Sandia, LLC, a wholly owned subsidiary of Honeywell International, Inc., for the U.S. Department of

Energy's National Nuclear Security Administration under Contract No. DE-NA-0003525.

J.P.M. and D.M. performed the central calculations and analysis presented in this work. S.M. initially guided the analysis of this work. The paper was written by J.P.M. and D.M., and S.M. contributed to writing the introduction and drawing the conclusions expressed in the paper.

Any subjective views or opinions that might be expressed in this paper do not necessarily represent the views of the U.S. Department of Energy or the U.S. Government.

- 
- [1] H. F. Wilson, O. Warschkow, N. A. Marks, N. J. Curson, S. R. Schofield, T. C. G. Reusch, M. W. Radny, P. V. Smith, D. R. McKenzie, and M. Y. Simmons, Thermal dissociation and desorption of  $\text{Ph}_3$  on Si(001): A reinterpretation of spectroscopic data, *Phys. Rev. B* **74**, 195310 (2006).
- [2] O. Warschkow, N. J. Curson, S. R. Schofield, N. A. Marks, H. F. Wilson, M. W. Radny, P. V. Smith, T. C. G. Reusch, D. R. McKenzie, and M. Y. Simmons, Reaction paths of phosphine dissociation on silicon (001), *J. Chem. Phys.* **144**, 014705 (2016).
- [3] M. Fuechsle, J. A. Miwa, S. Mahapatra, H. Ryu, S. Lee, O. Warschkow, L. C. L. Hollenberg, G. Klimeck, and M. Y. Simmons, A single-atom transistor, *Nat. Nanotechnol.* **7**, 242 (2012).
- [4] J. A. Ivie, Q. Campbell, J. C. Koepke, M. I. Brickson, P. A. Schultz, R. P. Muller, A. M. Mounce, D. R. Ward, M. S. Carroll, E. Bussmann, A. D. Baczewski, and S. Misra, Impact of incorporation kinetics on device fabrication with atomic precision, *Phys. Rev. Appl.* **16**, 054037 (2021).
- [5] J. Wyrick, X. Wang, P. Nambodiri, R. V. Kashid, F. Fei, J. Fox, and R. Silver, Enhanced atomic precision fabrication by adsorption of phosphine into engineered dangling bonds on H-Si using STM and DFT, *ACS Nano* **16**, 19114 (2022).
- [6] Q. Campbell, A. D. Baczewski, R. E. Butera, and S. Misra, Hole in one: Pathways to deterministic single-acceptor incorporation in Si(100)- $2 \times 1$ , *AVS Quantum Sci.* **4**, 016801 (2022).
- [7] K. E. J. Goh, L. Oberbeck, M. Y. Simmons, A. R. Hamilton, and M. J. Butcher, Influence of doping density on electronic transport in degenerate Si:P  $\delta$ -doped layers, *Phys. Rev. B* **73**, 035401 (2006).
- [8] B. Weber, S. Mahapatra, H. Ryu, S. Lee, A. Fuhrer, T. C. G. Reusch, D. L. Thompson, W. C. T. Lee, G. Klimeck, L. C. L. Hollenberg, and M. Y. Simmons, Ohm's law survives to the atomic scale, *Science* **335**, 64 (2012).
- [9] S. R. McKibbin, G. Scappucci, W. Pok, and M. Y. Simmons, Epitaxial top-gated atomic-scale silicon wire in a three-dimensional architecture, *Nanotechnology* **24**, 045303 (2013).
- [10] J. G. Keizer, S. R. McKibbin, and M. Y. Simmons, The impact of dopant segregation on the maximum carrier density in Si:P multilayers, *ACS Nano* **9**, 7080 (2015).
- [11] T. Škerek, S. A. Koester, B. Douhard, C. Fleischmann, and A. Fuhrer, Bipolar device fabrication using a scanning tunnelling microscope, *Nat. Electron.* **3**, 524 (2020).
- [12] K. J. Dwyer, S. Baek, A. Farzaneh, M. Dreyer, J. R. Williams, and R. E. Butera, B-doped  $\delta$ -layers and nanowires from area-selective deposition of  $\text{BCl}_3$  on Si(100), *ACS Appl. Mater. Interfaces* **13**, 41275 (2021).
- [13] S. Mahapatra, H. Büch, and M. Y. Simmons, Charge sensing of precisely positioned P donors in Si, *Nano Lett.* **11**, 4376 (2011).
- [14] M. G. House, E. Peretz, J. G. Keizer, S. J. Hile, and M. Y. Simmons, Single-charge detection by an atomic precision tunnel junction, *Appl. Phys. Lett.* **104**, 113111 (2014).
- [15] M. B. Donnelly, J. G. Keizer, Y. Chung, and M. Y. Simmons, Monolithic three-dimensional tuning of an atomically defined silicon tunnel junction, *Nano Lett.* **21**, 10092 (2021).
- [16] Y. He, S. K. Gorman, D. Keith, L. Kranz, J. G. Keizer, and M. Y. Simmons, A two-qubit gate between phosphorus donor electrons in silicon, *Nature* **571**, 371 (2019).
- [17] L. Kranz, S. K. Gorman, B. Thorgrimsson, Y. He, D. Keith, J. G. Keizer, and M. Y. Simmons, Exploiting a single-crystal environment to minimize the charge noise on qubits in silicon, *Adv. Mater.* **32**, 2003361 (2020).
- [18] F. Krauth, S. Gorman, Y. He, M. Jones, P. Macha, S. Kocsis, C. Chua, B. Voisin, S. Rogge, R. Rahman, Y. Chung, and M. Simmons, Flopping-mode electric dipole spin resonance in phosphorus donor qubits in silicon, *Phys. Rev. Appl.* **17**, 054006 (2022).
- [19] L. Fricke, S. J. Hile, L. Kranz, Y. Chung, Y. He, P. Pakkiam, M. G. House, J. G. Keizer, and M. Y. Simmons, Coherent control of a donor-molecule electron spin qubit in silicon, *Nat. Commun.* **12**, 3323 (2021).
- [20] X. Wang, E. Khatami, F. Fei, J. Wyrick, P. Nambodiri, R. Kashid, A. F. Rigosi, G. Bryant, and R. Silver, Experimental realization of an extended Fermi-Hubbard model using a 2D lattice of dopant-based quantum dots, *Nat. Commun.* **13**, 6824 (2022).
- [21] M. Kiczynski, S. K. Gorman, H. Geng, M. B. Donnelly, Y. Chung, Y. He, J. G. Keizer, and M. Y. Simmons, Engineering topological states in atom-based semiconductor quantum dots, *Nature* **606**, 694 (2022).
- [22] J. A. Haggmann, X. Wang, P. Nambodiri, J. Wyrick, R. Murray, M. D. Stewart, R. M. Silver, and C. A. Richter, High resolution thickness measurements of ultrathin Si:P monolayers using weak localization, *Appl. Phys. Lett.* **112**, 043102 (2018).
- [23] E. M. Anderson, D. M. Campbell, L. N. Maurer, A. D. Baczewski, M. T. Marshall, T.-M. Lu, P. Lu, L. A. Tracy, S. W. Schmucker, D. R. Ward, and S. Misra, Low thermal budget high-k/metal surface gate for buried donor-based devices, *J. Phys.: Mater.* **3**, 035002 (2020).
- [24] S. M. Sze and K. K. Ng, *Physics of Semiconductor Devices* (John Wiley & Sons, Hoboken, New Jersey, 2006).
- [25] P. Gehring, J. M. Thijssen, and H. S. J. van der Zant, Single-molecule quantum-transport phenomena in break junctions, *Nat. Rev. Phys.* **1**, 381 (2019).
- [26] D. K. Ferry, J. Weinbub, M. Nedjalkov, and S. Selberherr, A review of quantum transport in field-effect transistors, *Semicond. Sci. Technol.* **37**, 043001 (2022).
- [27] D. Mamaluy, M. Sabathil, and P. Vogl, Efficient method for the calculation of ballistic quantum transport, *J. Appl. Phys.* **93**, 4628 (2003).

- [28] D. Mamaluy, A. Mannargudi, D. Vasileska, M. Sabathil, and P. Vogl, Contact block reduction method and its application to a 10 nm MOSFET device, *Semicond. Sci. Technol.* **19**, S118 (2004).
- [29] M. Sabathil, D. Mamaluy, and P. Vogl, Prediction of a realistic quantum logic gate using the contact block reduction method, *Semicond. Sci. Technol.* **19**, S137 (2004).
- [30] D. Mamaluy, D. Vasileska, M. Sabathil, T. Zibold, and P. Vogl, Contact block reduction method for ballistic transport and carrier densities of open nanostructures, *Phys. Rev. B* **71**, 245321 (2005).
- [31] H. R. Khan, D. Mamaluy, and D. Vasileska, Quantum transport simulation of experimentally fabricated nano-FinFET, *IEEE Trans. Electron Devices* **54**, 784 (2007).
- [32] H. R. Khan, D. Mamaluy, and D. Vasileska, 3D NEGF quantum transport simulator for modeling ballistic transport in nano FinFETs, *J. Phys. Conf. Ser.* **107**, 012007 (2008).
- [33] X. Gao, D. Mamaluy, E. Nielsen, R. W. Young, A. Shirkorshidian, M. P. Lilly, N. C. Bishop, M. S. Carroll, and R. P. Muller, Efficient self-consistent quantum transport simulator for quantum devices, *J. Appl. Phys.* **115**, 133707 (2014).
- [34] J. P. Mendez, D. Mamaluy, X. Gao, and S. Misra, in *2021 International Conference on Simulation of Semiconductor Processes and Devices (SISPAD)* (IEEE, Dallas, TX, USA, 2021), p. 210.
- [35] J. Wang, A. Rahman, A. Ghosh, G. Klimeck, and M. Lundstrom, On the validity of the parabolic effective-mass approximation for the I-V calculation of silicon nanowire transistors, *IEEE Trans. Electron Devices* **52**, 1589 (2005).
- [36] N. Neophytou, A. Paul, M. S. Lundstrom, and G. Klimeck, Simulations of nanowire transistors: atomistic vs. effective mass models, *J. Comput. Electron.* **7**, 363 (2008).
- [37] See Supplementary Material at <http://link.aps.org/supplemental/10.1103/PhysRevApplied.20.054021> for further information.
- [38] J. P. Mendez and D. Mamaluy, Conductivity and size quantization effects in semiconductor  $\delta$ -layer systems, *Sci. Rep.* **12**, 16397 (2022).
- [39] S. Lee, H. Ryu, H. Campbell, L. C. L. Hollenberg, M. Y. Simmons, and G. Klimeck, Electronic structure of realistically extended atomistically resolved disordered Si:P  $\delta$ -doped layers, *Phys. Rev. B* **84**, 205309 (2011).
- [40] F. Mazzola, C. M. Polley, J. A. Miwa, M. Y. Simmons, and J. W. Wells, Disentangling phonon and impurity interactions in  $\delta$ -doped Si(001), *Appl. Phys. Lett.* **104**, 173108 (2014).
- [41] L. V. Keldysh, Diagram technique for nonequilibrium processes, *Sov. Phys. J. Exp. Theor. Phys.* **20**, 1018 (1965).
- [42] S. Datta, *Electronic Transport in Mesoscopic Systems* (Cambridge university press, Cambridge, 1997).
- [43] J. P. Mendez, D. Mamaluy, X. Gao, E. M. Anderson, D. M. Campbell, J. A. Ivie, T.-M. Lu, S. W. Schmucker, and S. Misra, in *2020 International Conference on Simulation of Semiconductor Processes and Devices (SISPAD)* (IEEE, Kobe, Japan, 2020), p. 181.
- [44] D. Mamaluy, J. P. Mendez, X. Gao, and S. Misra, Revealing quantum effects in highly conductive  $\delta$ -layer systems, *Commun. Phys.* **4**, 205 (2021).
- [45] K. E. J. Goh and M. Y. Simmons, Impact of Si growth rate on coherent electron transport in Si:P delta-doped devices, *Appl. Phys. Lett.* **95**, 142104 (2009).
- [46] T. C. G. Reusch, K. E. J. Goh, W. Pok, W.-C. N. Lo, S. R. McKibbin, and M. Y. Simmons, Morphology and electrical conduction of Si:P  $\delta$ -doped layers on vicinal Si(001), *J. Appl. Phys.* **104**, 066104 (2008).
- [47] S. R. McKibbin, C. M. Polley, G. Scappucci, J. G. Keizer, and M. Y. Simmons, Low resistivity, super-saturation phosphorus-in-silicon monolayer doping, *Appl. Phys. Lett.* **104**, 123502 (2014).
- [48] M. B. Donnelly, M. M. Munia, J. G. Keizer, Y. Chung, A. M. S.-E. Huq, E. N. Osika, Y.-L. Hsueh, R. Rahman, and M. Y. Simmons, Multi-scale modeling of tunneling in nanoscale atomically precise Si:P tunnel junctions, *Adv. Funct. Mater.* **33**, 2214011 (2023).
- [49] J. P. Perdew and A. Zunger, Self-interaction correction to density-functional approximations for many-electron systems, *Phys. Rev. B* **23**, 5048 (1981).
- [50] A. J. Holt, S. K. Mahatha, R.-M. Stan, F. S. Strand, T. Nyborg, D. Curcio, A. K. Schenk, S. P. Cooil, M. Bianchi, J. W. Wells, P. Hofmann, and J. A. Miwa, Observation and origin of the  $\Delta$  manifold in Si:P  $\delta$  layers, *Phys. Rev. B* **101**, 121402 (2020).
- [51] F. Mazzola, C.-Y. Chen, R. Rahman, X.-G. Zhu, C. M. Polley, T. Balasubramanian, P. D. King, P. Hofmann, J. A. Miwa, and J. W. Wells, The sub-band structure of atomically sharp dopant profiles in silicon, *npj Quantum Mater.* **5**, 34 (2020).
- [52] K. Shoorideh and C. O. Chui, On the origin of enhanced sensitivity in nanoscale FET-based biosensors, *Proc. Natl. Acad. Sci.* **111**, 5111 (2014).